The Astrophysical Journal, 1007:162 (12pp), 2026 August 20 https://doi.org/10.3847/1538-4357/ae7327
© 2026. The Author(s). Published by the American Astronomical Society.
OPEN ACCESS

Stellar Interpretation of Meteoritic Data and PLotting for Everyone (SIMPLE): Isotope Mixing Lines for Six Sets of Core-collapse Supernova Models

Marco Pignatari[1,2,3], Mattias Ek[4], Georgy V. Makhatadze[1,2,5,6], Gábor G. Balázs[1,2,7], Lorenzo Roberti[1,2,10,21], James M. Ball[4], Borbála Cseh[1,2,9], Alessandro Chieffi[10,11,12], Chris Fryer[13], Falk Herwig[14], Chiara Incollingo[4], Thomas Lawson[15], Marco Limongi[8,10,16], Thomas Rauscher[17,18], Maria Schönbächler[4], Andre Sieverding[19], Reto Trappitsch[20], and Maria Lugaro[1,2,7,12]

[1] Konkoly Observatory, HUN-REN Research Centre for Astronomy and Earth Sciences, H-1121 Budapest, Konkoly Thege M. út 15-17, Hungary; marco.pignatari@csfk.org, maria.lugaro@csfk.org
[2] CSFK, MTA Centre of Excellence, Budapest, Konkoly Thege Miklós út 15–17, H-1121, Hungary
[3] University of Bayreuth, BGI, Universitätsstraße 30, 95447 Bayreuth, Germany
[4] Institute for Geochemistry and Petrology, ETH Zürich, Zurich, Switzerland; mattias.ek@eaps.ethz.ch
[5] Université Paris Cité, Institut de Physique du Globe de Paris, CNRS, 1 rue Jussieu, Paris 75005, France
[6] Centre for Star and Planet Formation (StarPlan), Globe Institute, Faculty of Health and Medical Sciences, University of Copenhagen, Øster Voldgade 5–7, 1350 Copenhagen K, Denmark
[7] ELTE Eötvös Loránd University, Institute of Physics and Astronomy, Budapest 1117, Pázmány Péter sétány 1/A, Hungary
[8] Istituto Nazionale di Astrofisica—Osservatorio Astronomico di Roma (INAF—OAR), Via Frascati 33, I-00040, Monteporzio Catone, Italy
[9] MTA-ELTE Lendület "Momentum" Milky Way Research Group, Hungary
[10] Istituto Nazionale di Fisica Nucleare—Sezione di Perugia (INFN), via A. Pascoli s/n, I-06125 Perugia, Italy
[11] Istituto Nazionale di Astrofisica—Istituto di Astrofisica e Planetologia Spaziali (INAF—IAPS), Via Fosso del Cavaliere 100, I-00133, Roma, Italy
[12] School of Physics and Astronomy, Monash University, VIC 3800, Australia
[13] Center for Nonlinear Studies, Los Alamos National Laboratory, Los Alamos, NM 87545, USA
[14] Astronomy Research Centre, Department of Physics & Astronomy, University of Victoria, Victoria, BC V8W 2Y2, Canada
[15] E. A. Milne Centre for Astrophysics, University of Hull, Cottingham Road, Kingston upon Hull, HU6 7RX, UK
[16] Kavli Institute for the Physics and Mathematics of the Universe, Todai Institutes for Advanced Study, University of Tokyo, Kashiwa, 277-8583 (Kavli IPMU, WPI), Japan
[17] Department of Physics, University of Basel, Klingelbergstr. 82, CH-4056 Basel, Switzerland
[18] Centre for Astrophysics Research, University of Hertfordshire, Hatfield AL10 9AB, UK
[19] Lawrence Livermore National Laboratory, P.O. Box 808, L-414, Livermore, California 94551, USA
[20] Laboratory for Biological Geochemistry, School of Architecture, Civil & Environmental Engineering, École Polytechnique Fédérale de Lausanne, GR C2 505, Station 2, 1015 Lausanne, Switzerland
[21] INAF—Osservatorio Astronomico di Palermo, Piazza del Parlamento 1, I-90134 Palermo, Italy
Received 2026 February 3; revised 2026 May 6; accepted 2026 May 8; published 2026 August 14

Abstract

Bulk meteorites and their inclusions exhibit, for many chemical elements, isotopic variability produced by nucleosynthetic events in stars and supernovae before the formation of the Sun. While the exact astrophysical origins of these variations are still a matter of debate, their identification provides insights into the environment of the Sun's birth and the formation of the solar system. Here, we present a new Python tool called Stellar Interpretation of Meteoritic Data and Plotting for Everyone (SIMPLE) designed to compare the isotopic composition of the ejecta from core-collapse supernovae (CCSNe) with meteoritic data. In the present version, the SIMPLE toolkit includes a dataset of 18 CCSN models from six different published sets, with initial masses of 15, 20, and 25 $M_{\odot}$ and solar metallicity. SIMPLE is designed to easily extract the isotopic abundances predicted by each CCSN model for any elements and postprocess them into the format needed to compare to the meteoritic data, therefore facilitating their interpretation. As an example of how to use SIMPLE, we analyze the composition of the Ni isotopes in the 18 models and confirm that bulk meteorite Ni anomalies are compatible with material from the innermost Si-rich region of CCSN ejecta. Designed as a collaborative platform, SIMPLE is open source and welcomes community contributions to enhance its development and dissemination for stellar nucleosynthesis and meteoritic studies. Future enhancements include the addition of more model predictions and the inclusion of mixing between different layers of supernova ejecta.

Unified Astronomy Thesaurus concepts: Massive stars (732); Core-collapse supernovae (304); Isotopic abundances (867); Meteorite composition (1037); Stellar processes (1623)

1. Introduction

Materials derived from early solar system bodies and dust reservoirs exhibit a nucleosynthetic isotope variability across many chemical elements. These include elements of vastly different nucleosynthetic heritage, such as alpha (J. I. Simon et al. 2009), iron peak (M. Rotaru et al. 1992), and neutron-capture elements (N. Dauphas et al. 2002). The variability is typically revealed by isotopic analysis of bulk meteorites and their components, such as calcium-aluminum-rich inclusions (CAIs; S. Niemeyer & G. W. Lugmair 1981). The origin of the solar system heterogeneity is elusive, and several models have been proposed, which can be divided into two major groups and may both apply depending on the element and variation

Original content from this work may be used under the terms of the Creative Commons Attribution 4.0 licence. Any further distribution of this work must maintain attribution to the author(s) and the title of the work, journal citation and DOI.

considered. The heterogeneity could have been a product of separation of the anomalous carriers based on their thermal (A. Trinquier et al. 2009; M. Ek et al. 2020) and/or aerodynamic (R. C. J. Steele et al. 2012; M. A. Hutchison et al. 2022) properties. Alternatively, it could have been imprinted from a heterogeneous parental molecular cloud (J. A. M. Nanne et al. 2019) or directly by a nearby supernova (L. Qin et al. 2011; G. A. Brennecka et al. 2013; T. Iizuka et al. 2025). Some models propose a combination of the two to explain different trends observed in the inner and outer solar system (E. M. M. E. Van Kooten et al. 2016). Studying the nucleosynthetic variability of the solar system can help constrain processes such as planetesimal (T. Lichtenberg et al. 2021) and planet (W. Akram & M. Schönbächler 2016; T. S. Kruijer et al. 2017; M. Schiller et al. 2018; C. Burkhardt et al. 2021) formation, dust migration (E. van Kooten et al. 2021), and evolution (M. Ek et al. 2020) in the protoplanetary disk and infall dynamics from the parental molecular cloud (E. M. M. E. Van Kooten et al. 2016; J. A. M. Nanne et al. 2019). While further information can be found in many recent reviews (N. Dauphas & E. A. Schauble 2016; L. Qin & R. W. Carlson 2016; T. Yokoyama & R. J. Walker 2016; K. R. Bermingham et al. 2020; T. Kleine et al. 2020; T. S. Kruijer et al. 2020; K. Mezger et al. 2020; K. Bermingham & B. Meyer 2024; N. Liu et al. 2024; M. Bizzarro et al. 2025; M. Schönbächler et al. 2025; F. L. H. Tissot et al. 2025), caution is advised as the field is developing at a fast pace.

One of the steps required to understand the variability and exploit it to study the early solar system is the identification of the nucleosynthetic inventory carried by various materials in the early solar system and, especially, which components could have been distributed heterogeneously and why. This requires a detailed comparison between the meteoritic isotope data and the predictions from models of stellar nucleosynthesis. The common approach to compare the meteorite data to the predictions of stellar nucleosynthesis is to plot a mixing line between the bulk solar system and the stellar component in question, which should pass through the data when the stellar component is diluted by the bulk solar system (assumed to be the terrestrial) isotopic composition. While mixing-line calculations are simple, in the case of extremely different isotope compositions, such as the case with the products of nucleosynthesis, the aforementioned internal normalization introduces nonlinear effects, and special care must be taken to avoid creating artifacts in the data. The comparison task is further complicated for a number of reasons, including the specifics of data reduction employed in isotope studies of bulk meteorites, the fact that the measured isotopic ratios reflect the complex history of the chemical and nuclear reactions that altered the sample and its precursor material, and the many stellar and nuclear physics uncertainties carried by the model predictions.

In relation to the laboratory data, the typical magnitude of the isotope effects induced by chemical reactions is of the order of 10^{-3}, while the resolved stellar nucleosynthetic effects on a bulk meteorite can be as low as 10^{-6}. As such, separating the effects caused by nucleosynthesis from those caused by chemical and other nuclear processes can be a nontrivial task. Most chemical processes affect isotope compositions in a mass-dependent manner, which can be routinely corrected for using mass-dependent fractionation laws, resulting in a mass-independent isotope composition (W. A. Russell et al. 1978). Chemical mass-independent isotope fractionation is also possible; however, typically, these effects are limited to a few chemical elements (N. Dauphas & E. A. Schauble 2016). In situ nuclear reactions, such as radioactive decay and nuclear reactions induced by exposure to cosmic rays, result in mass-independent isotope effects as well, and correction for these is sometimes needed too.

In relation to the stellar models, the full availability of data from model predictions is limited, especially in the case of core-collapse supernovae (CCSNe). These represent the final explosion of massive stars (with initial masses roughly >9–10 $M_{\odot}$, e.g., M. Limongi et al. 2024) and are of particular interest in relation to the comparison to meteoritic data for a number of reasons. The main astrophysical reasons are that (i) they derive from massive stars, therefore their progenitors have relatively short lifetimes (from a few to a few tens of Myr). Therefore, they could have exploded in the same molecular cloud, or even the same stellar cluster, where the Sun was born. (ii) They are observed to produce dust, some of which has been found in the meteoritic stardust inventory. Probably up to 30% of all the presolar stardust originally present in the presolar nebula originated from these explosions (P. Hoppe et al. 2022). This dust is a likely candidate to have trapped the nucleosynthetic anomalies of the ejecta of their parent stars and carried them into the early solar system.

Moreover, CCSN ejecta carry the composition produced by a large variety of nuclear-burning processes, from signatures of the hydrostatic nucleosynthesis that happened in the stellar supernova progenitor to the signature of the following explosive nucleosynthesis. While this diversity should be fully exploited to try to explain the observations, an especially crucial aspect of the comparison is represented by the analysis of the composition of individual parts of the ejecta, carrying their specific isotopic signatures. Analysis of the composition of each ejected shell is needed because CCSN ejecta are not fully mixed (as in the case of the winds from the fully convective envelopes of asymptotic giant branch (AGB) stars); therefore, dust can form locally. Evidence of this is the existence of meteoritic stardust grains, whose composition typically carries the signature of limited mixing between one or two different parts of the CCSN ejecta (e.g., M. Pignatari et al. 2013; E. Zinner 2014). The comparison between the composition of different CCSN shells and meteoritic data, however, has only been sparsely explored (R. C. J. Steele et al. 2012; T. Hopp et al. 2022). This is because, for this task, the abundance profiles versus ejected mass are needed, which are usually not published or not as easily accessible as the total integrated stellar yields. It follows that only a few models have been used for such an analysis so far (B. S. Meyer et al. 1995; T. Rauscher et al. 2002; S. E. Woosley & A. Heger 2007), which cannot capture the progress made in the past two decades on our understanding of CCSN nucleosynthesis.

Model uncertainties stemming from nuclear and stellar physics are still large, especially as detailed nucleosynthesis is mostly available from one-dimensional (1D) models for both the progenitor and the explosion, although major efforts have been made and are under way to improve the situation; see the recent review by C. L. Fryer et al. (2026), as well as, e.g., A. Burrows & D. Vartanyan (2021) and L. Boccioli & L. Roberti (2024), and references therein. Nevertheless, considering different sets of models computed independently can help to evaluate systematic uncertainties at least in a qualitative way and establish which features of CCSN nucleosynthesis are robust, i.e., potentially mostly depending

on the nuclear physics properties of the burning that produce them, and which features are instead model dependent.

To advance on this task and support the common effort of the comparison between data and models, we developed a Python tool called Stellar Interpretation of Meteoritic Data and PLotting for Everyone (SIMPLE), which currently reads 18 CCSN models of masses 15, 20, and 25 $M_{\odot}$ from six different published sets, spanning from the popular models by T. Rauscher et al. (2002) to more recent models published from 2016 to 2022. The code includes a routine for calculating the correlations between isotopic ratios predicted by the models as a function of the ejected mass to be directly compared to the meteoritic observations. The code can be downloaded as a Python package and therefore can also be modified by each user as needed. Meetings and collaborations are envisaged for users so that we can share developments.

We note that the models available in SIMPLE are all Fe-CCSNe, i.e., none of them represent explosions from core collapse driven by electron captures (ECs) in stars of lower masses ($\sim$9 $M_{\odot}$). While these EC supernovae (ECSNe) are a popular option to explain ^{48}Ca excesses in bulk meteorites (e.g., N. Dauphas et al. 2014; L. R. Nittler et al. 2018), their existence and occurrence at solar metallicity, their potential for dust production, and the large nuclear uncertainties affecting their ejecta are currently strongly debated (e.g., S. Jones et al. 2019a, 2019b; J. den Hartogh et al. 2022). This type of supernova will therefore be addressed in future works, together with developments on CCSN nucleosynthesis from three-dimensional (3D) simulations and improved nuclear and neutrino input physics. The SIMPLE tool developed and presented here is able to incorporate future and updated models.

The paper is structured as follows: in Section 2, we describe the structure and workings of the SIMPLE code; in Section 3, we describe the 18 CCSN models currently readable by the code. In Section 4, we present some example cases of the usage of the code, focusing on the Ni isotopes. In Section 5, we summarize and discuss our work and describe related future work.

2. Methods

In this section, we describe the main properties of the SIMPLE code, which allows comparison of CCSN abundances with bulk meteoritic data. The code can be downloaded from GitHub,[22] and documentation and tutorials for the code are also available.[23] The code is also available on the Python Package Index (`pip install simple-chetec`). This study used v0.4.4 of the code, archived on Zenodo (doi:10.5281/zenodo.19110452). The stellar input data are available separately on Zenodo (doi:10.5281/zenodo.19063105, v3.1), where they can be updated as needed. Below, we briefly describe the code functionalities.

Reading the tabulated abundances. The files that contain the tables for each model with the abundance of all the isotopes just after the explosion (see Section 3 for details) as a function of location in the mass of the ejecta are provided at zenodo.org/records/19063105. Isotopic abundances for each isotope i are usually provided by CCSN modelers in mass fractions X_i.[24] These can be directly used to calculate the total yield for each isotope via integrating the product of the mass fraction and the mass of each resolved shell over the whole ejected mass. When divided by their mass, each isotopic mass fraction X_i is converted into $Y_i = X_i/A_i$, the molar fraction of the isotope, or the "normalized" abundance by number. The Y_i and X_i quantities are not equivalent to use for normalization: they should match the same quantity at which the solar/terrestrial/standard abundances are given. Otherwise, for any ratio of any isotope i over j, a factor A_i/A_j is wrongly introduced to the calculations. Moreover, calculation of radioactive decay and addition of possible chemistry fractionation effects (see below) must be done in molar fractions. Therefore, the code is designed to be flexible in converting the data from mass fractions to molar fractions and vice versa, using the approximated masses, i.e., using mass 56 for ^{56}Ni instead of 55.942, etc. The code works self-consistently with either representation, as chosen by the user. To avoid confusion, an attribute is associated with the data "mass" for mass fraction and "mole" for the abundance. As detailed in Section 3, not all the elements and isotopes are available in all the models, and the code will issue a warning in case of missing isotopes. Also implemented is the possibility to include, in each figure where the x-axis represents the mass coordinate, separation lines and labels indicating the zonal structure according to the most abundant burning products, following B. S. Meyer et al. (1995).

Solar/terrestrial/standard abundances. To normalize stellar model predictions, we cannot use the laboratory standards used to normalize the experimental data. Instead, stellar isotopic variations need to be calculated relative to their own "standard" abundances, i.e., the initial abundances used in each model. If different numbers are used, fictional anomalies may appear that are not due to nuclear burning but to the difference between the initial values used in the stellar model calculations and the different values used. As the initial abundances are different for each sets of models (Section 3), and their tabulated values include a different number of digits, the initial abundances used during the computation of each stellar model is automatically used as the standard abundance for all normalization procedures.

Radioactive nuclei. While creating the abundance tables of selected isotopes to analyze, the user can decide, case by case, how to handle adding the abundances of radioactive nuclei into those of their stable daughter nuclei. The current version of the code does not yet include a radioactive decay routine; therefore, the abundances of radioactive nuclei can only be omitted completely or added in their entirety to the abundance of their stable daughter nuclei. Once an element or isotope system is selected to be studied by the user, a preliminary step for the analysis is to decide which radioactive isotopes should be added to each stable isotopes. The stellar abundances are given relatively soon after the explosion (at most after $\sim$7 hr; see Section 3); therefore, most radioactive nuclei need to be added if the user wishes to assume that they were incorporated into dust, given that dust formation timescales in CCSNe are of the order of months to years (E. S. Brooker et al. 2022). If a user requests a radioactive isotope that is not included in a model, the abundance of this isotope is automatically set to zero. An example is shown in Table 1, which lists the radioactive nuclei to be considered for the Ni isotopes. In this case, all the radioactive isotopes can be safely added to their respective stable daughter nucleus, given their short half-lives, except for the case of ^{60}Fe, which needs a more careful analysis because it may or may not be incorporated in the same dust as Ni. In this case, it is interesting to compare the ^{60}Ni abundance, with and without the inclusion of ^{60}Fe, as done

[22] https://github.com/mattias-ek/SIMPLE

[23] https://mattias-ek.github.io/SIMPLE/

[24] This corresponds to $n_i \times m_i/\rho = N_i \times m_i/M$, where $m_i = A \times amu$ is the mass of species i, $n_i = N_i/V$, i.e., the total number of nuclei N_i per unit volume, ρ is the total density, and M is the total mass. By definition, $\Sigma_i X_i = 1$.

Table 1
List of the Radioactive Isotopes Whose Abundances Were Added to Those of the Corresponding Stable Ni Isotopes to Produce Figures 2 and 3

Stable Isotope	Unstable Isotope	Half-life	Decay Mode
^{58}Ni	^{58}Cu	(3.204 ± 0.007) s	β^+
^{60}Ni	^{60}Cu	(23.7 ± 0.4) ms	β^+
	^{60}Zn	(2.38 ± 0.05) ms	β^+
	^{60}Co	(1925.28 ± 0.14) d	β^-
	^{60}Fe	(2.62 ± 0.04) Myr	β^-
^{61}Ni	^{61}Cu	(3.339 ± 0.008) h	β^+
	^{61}Zn	(89.1 ± 0.2) s	β^+
	^{61}Co	(1.649 ± 0.005) h	β^-
	^{61}Fe	(5.98 ± 0.06) ms	β^-
^{62}Ni	^{62}Cu	(9.673 m ± 0.008) ms	β^+
	^{62}Zn	(9.186 ± 0.013) h	β^+
	^{62}Co	(1.5 ± 0.4) ms	β^+
	^{62}Fe	(68 ± 2) s	β^-
^{64}Ni	^{64}Cu	(12.701 ± 0.002) hr	β^-

Note. Their decay mode and half-lives are also indicated, the latter in units of milliseconds (ms), seconds (s), hours (h), days (d), and million years (Myr) and with 1σ error (from https://www.nndc.bnl.gov/nudat3/).

in Figure 1 for a 20 $M_\odot$ model by C. Ritter et al. (2018b) (from the model set Ri18, see Section 3.4). Except for this figure, all the results presented in Section 4 are calculated using abundances where all the radioactive isotopes are fully decayed.

Dilution and internal normalization. For comparison to the meteoritic data, the stellar ejecta need to be diluted, internally normalized, and expressed as ε values, i.e., per 10,000 deviations relative to the initial stellar abundances, as described above (see the full derivation, e.g., in M. Lugaro et al. 2023). For example, let us consider the isotope abundance profiles shown in Figure 2 for the 20 $M_\odot$ models from the different model sets considered in this work (see Section 3 for details). For these abundances and in the case of $\varepsilon\,^{64}\mathrm{Ni}^{*}_{(81)}$ in Figures 3, and 4, the * is used just to indicate that all the radioactive isotopes are fully decayed (see the previous subsection), and

$$\varepsilon^{64}\mathrm{Ni}_{(81)} = \left(\frac{(^{64}\mathrm{Ni}/^{61}\mathrm{Ni})^{\mathrm{norm}}}{(^{64}\mathrm{Ni}/^{61}\mathrm{Ni})^{\mathrm{init}}} - 1 \right) \times 10^4, \quad (1)$$

where $(^{64}\mathrm{Ni}/^{61}\mathrm{Ni})^{\mathrm{init}}$ is the initial stellar ratio used in each model, and $(^{64}\mathrm{Ni}/^{61}\mathrm{Ni})^{\mathrm{norm}}$ is the ratio internally normalized using $^{58}\mathrm{Ni}/^{61}\mathrm{Ni}$, i.e.,

$$(^{64}\mathrm{Ni}/^{61}\mathrm{Ni})^{\mathrm{norm}} = (^{64}\mathrm{Ni}/^{61}\mathrm{Ni})^{\mathrm{dil}} \left(\frac{(^{58}\mathrm{Ni}/^{61}\mathrm{Ni})^{\mathrm{dil}}}{(^{58}\mathrm{Ni}/^{61}\mathrm{Ni})^{\mathrm{dil}}} \right)^{-Q}. \quad (2)$$

Here,

$$Q = \frac{\ln(64) - \ln(61)}{\ln(58) - \ln(61)} \sim \frac{64 - 61}{58 - 61}, \quad (3)$$

and $(^{64}\mathrm{Ni}/^{61}\mathrm{Ni})^{\mathrm{dil}}$ and $(^{58}\mathrm{Ni}/^{61}\mathrm{Ni})^{\mathrm{dil}}$ are the isotopic ratios derived after dilution of the stellar abundances with the solar abundances[25] and using the free parameter x as the dilution factor, i.e.,

$$^{64}\mathrm{Ni} = {}^{64}\mathrm{Ni}_\odot + (\,{}^{64}\mathrm{Ni}^{\mathrm{star}} \times x). \quad (4)$$

This dilution (or linearization) is necessary, as the mixing lines between the internally normalized solar system and the extremely anomalous compositions of the stellar nucleosynthetic predictions are not straight, as one might expect, due to the effects introduced by the exponential law used for the normalization. These effects are only negligible in the case of the relatively similar mixing end-member isotope compositions. To perform this transformation, the default method used by the code dilutes the stellar abundances such that the largest offset from the model initial abundances among all the isotopic ratios calculated from all the selected isotopes corresponds to an ε value of ± 1. This value can be adjusted by the user, and the corresponding dilution factor can be extracted. A minimum value of the dilution factor can also be set, which helps to avoid spurious results that can occur when the abundances (for example, in the H-rich envelope where not much nuclear burning happened) are too close to the initial values. For comparison, the linear approximation method from N. Dauphas et al. (2004) is also implemented in the code, including the choice of approximating the Q value using masses instead of ln(masses) (see Equation (3)).

Chemical fractionation. When using SIMPLE to plot isotopic ratios of two different elements against each other, it is possible to apply chemical enrichment factors to simulate chemical fractionation, i.e., elemental separation according to chemical properties, which changes the elemental relative abundances and therefore the relative dilution. This can be done in two ways: either the abundances can be modified using enrichment factors as multiplication factors to the stellar abundances, or the relative abundances of chemical elements can be set to given, fixed values (e.g., corresponding to the relative proportions of Mg and Al in spinel).

Validation test. To check that the code works properly, we compared the results for the Ni isotopes to those published by R. C. J. Steele et al. (2012) in their Figure 9 (top panels) using

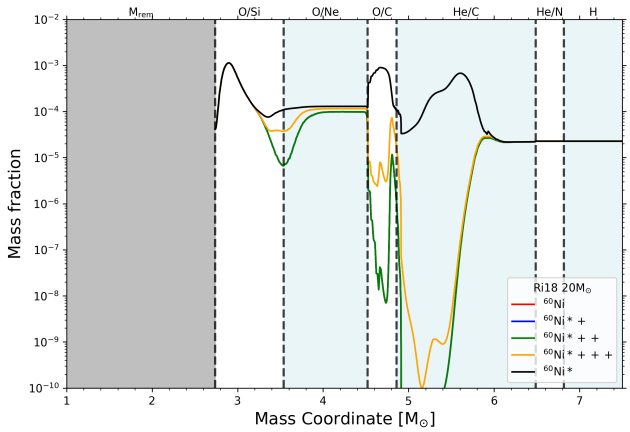

Figure 1. Mass fraction (mass) of ^{60}Ni as a function of the mass coordinate of the ejecta for the 20 $M_\odot$ model of Ri18, with the different ejecta layers also indicated. The ^{60}Ni abundance is calculated by progressively adding the abundances of the four radioactive isotopes listed in Table 1. In the label box, "^{60}Ni" corresponds to no radiogenic contributions, "^{60}Ni* +" to the addition of ^{60}Cu, "^{60}Ni* + +" also of ^{60}Zn, and "^{60}Ni* + + +" also of ^{60}Co. ^{60}Ni* includes all the previous isotopes plus ^{60}Fe, therefore corresponding to the same line plotted in Figure 2. Note that the red, blue, and green lines overlap, which means that only ^{60}Co and ^{60}Fe would contribute to the abundance of ^{60}Ni in this model.

[25] Here, these also correspond to the initial stellar abundances, but they are conceptually different as they would need to be scaled if models of different metallicity are considered.

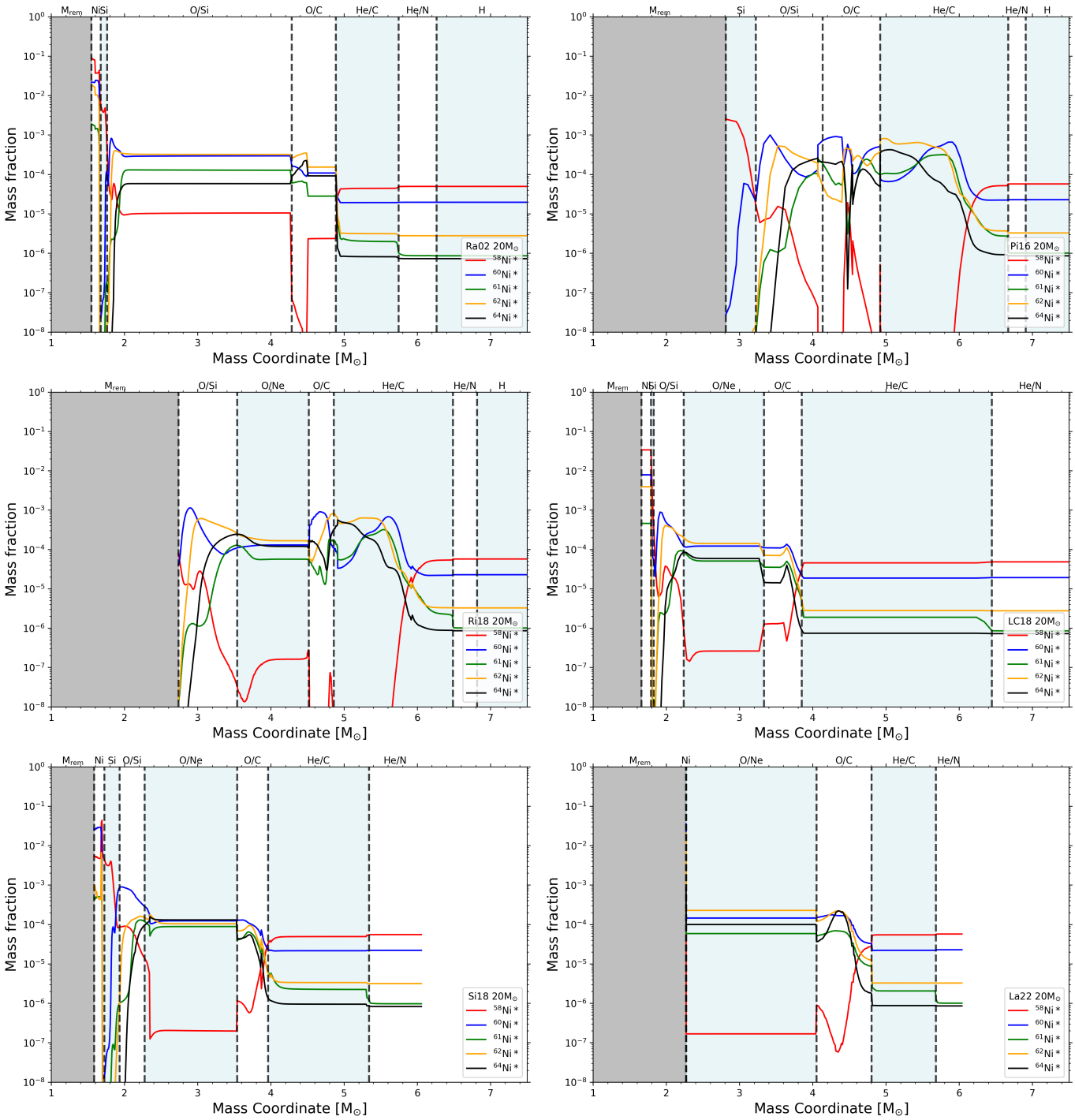

Figure 2. Abundance profiles (in mass fraction (mass)) of all the stable Ni isotopes (different colors, as indicated in the legend box) as a function of the mass coordinate of the ejecta for the 20 $M_{\odot}$ CCSN models of the six sets described in Section 3. Each set is indicated in the label box of each panel. Each model is separated into the different zone characterized by the most abundant burning products according to the classification of B. S. Meyer et al. (1995). Radiogenic production contributing to each isotope (according to Table 1) is included in each abundance. No abundances are reported in the database for the gray area at the lowest mass coordinates, given that this area is not part of the ejecta but of the remnant, compact object. The stellar surface is also not shown, as the composition remains constant in the H-rich region. Note that, in Si18 and La22, the explosion is only followed up to a peak temperature of $\sim$1.5 GK; therefore, these models only include the zones up to the He/N. In all the other cases, the envelope of the star is included in the simulation dominion, and also the H zone is provided.

the 25 $M_{\odot}$ model from T. Rauscher et al. (2002), which is also included in our dataset. We found that our results are in agreement with those published only when using a different model, from the T. Rauscher et al. (2002) set, than the model labeled "a28" in our dataset, which was calculated with the standard choice of the ^{22}Ne(α,n)^{25}Mg reaction rate defined in that paper. Other small differences also present are attributable to the use of different abundance quantities and to spurious results in the stellar envelope due to the choice of the solar/terrestrial abundances (see the discussion above).

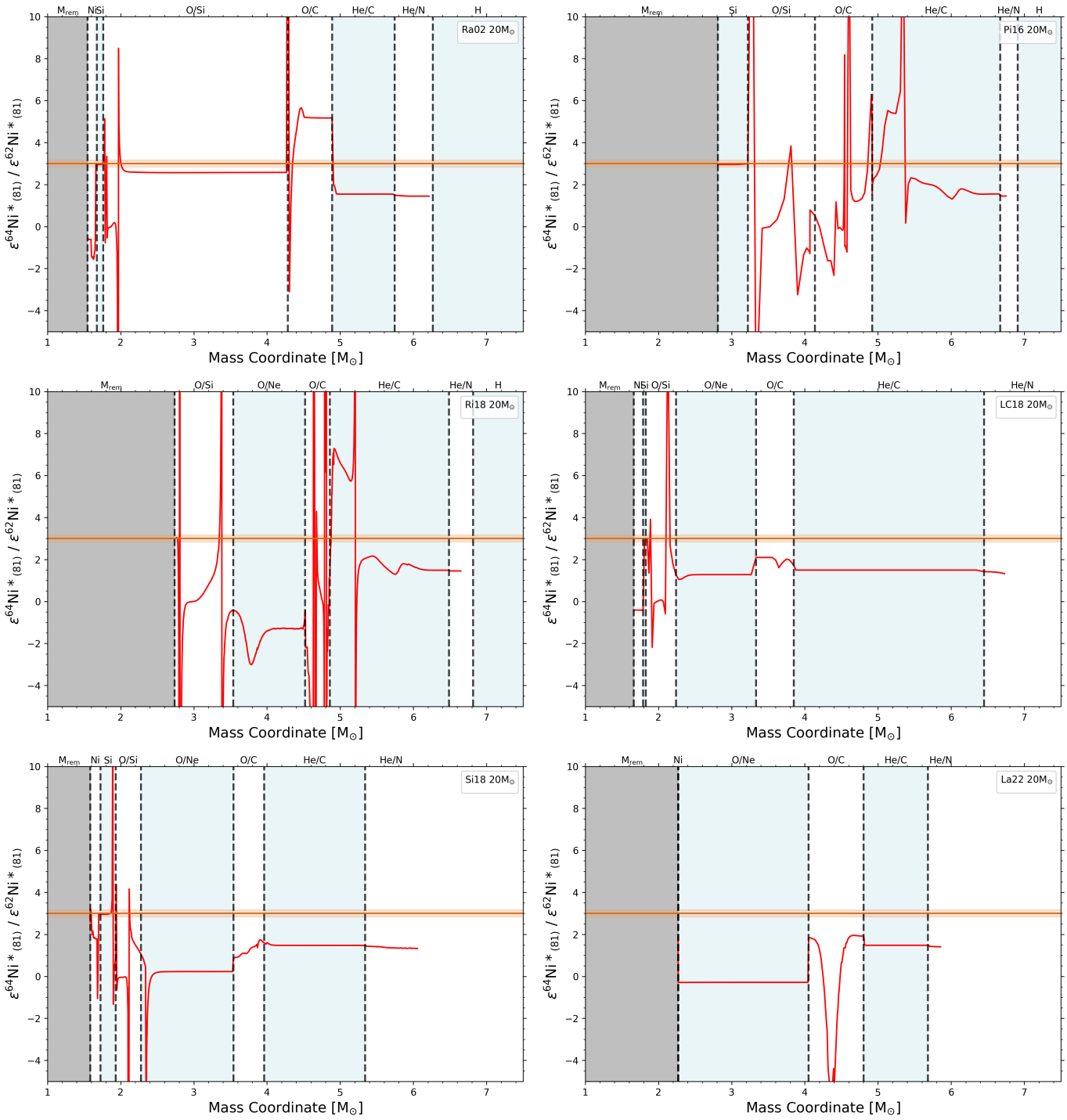

Figure 3. The predicted slope of $\varepsilon^{64}\mathrm{Ni}_{(81)}$ versus $\varepsilon^{62}\mathrm{Ni}_{(81)}$ internally normalized to $^{58}\mathrm{Ni}/^{61}\mathrm{Ni}$, as indicated by the last digit of their masses in the subscript bracket (81) of the y-axis label, and where the asterisks indicate that all the radioactive isotopes are decayed into their corresponding stable daughter, calculated from the abundances shown in Figure 2. The slope reported by R. C. J. Steele et al. (2012) of 3.003 ± 0.166 from bulk meteoritic data is indicated for comparison as the horizontal orange line, with the shaded region representing the uncertainty.

3. Models

The SIMPLE package includes six sets of CCSN models, each including three stars with initial masses of 15, 20, and 25 $M_{\odot}$ and solar metallicity, for a total of 18 models. Out of these sets of models, only one (T. Rauscher et al. 2002) has so far been extensively used for comparison to data from meteoritic bulk rocks and inclusions. The other model mostly used so far has been the 25 $M_{\odot}$ model published by B. S. Meyer et al. (1995), which was calculated using the same stellar evolution code and explosion mechanism as T. Rauscher et al. (2002)'s models (see the details in the next subsection). Table 2 lists the different sets and their acronyms in alphabetical order. The main features of each set are described in the following subsections (listed in chronological order, as references are often needed from one set to the following). All the stellar progenitors are nonrotating stars, and the exact value of the solar metallicity and the initial isotopic distribution depends on the set and are reported in detail below.

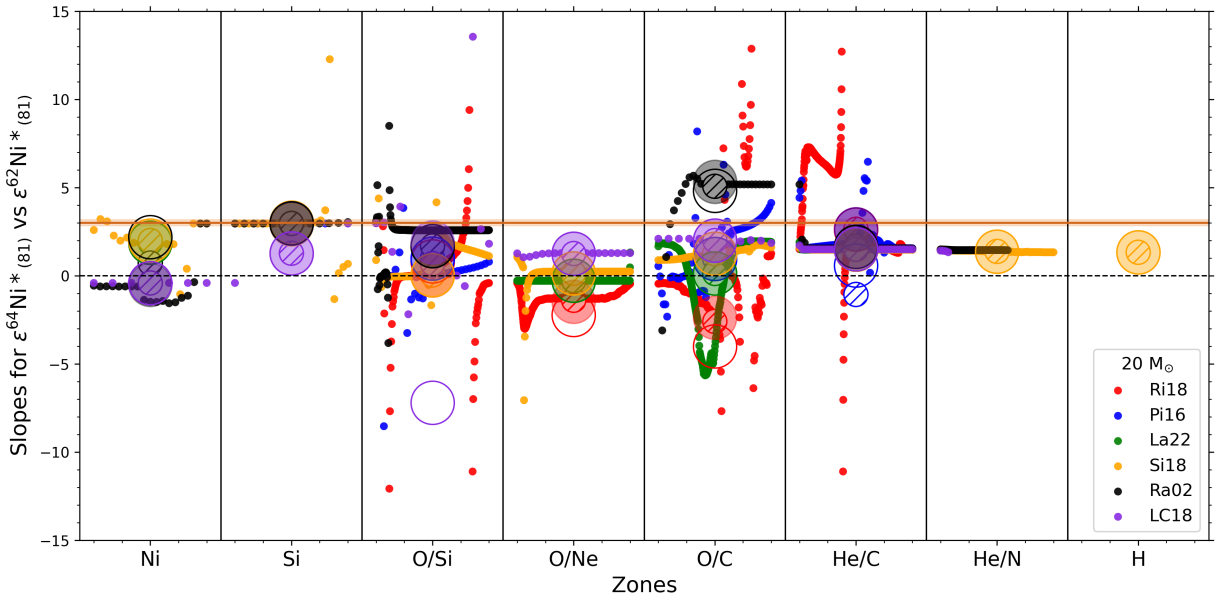

Figure 4. Summary of all the predicted slopes of $\varepsilon^{64}Ni_{(81)}$ versus $\varepsilon^{62}Ni_{(81)}$, internally normalized to $^{58}Ni/^{61}Ni$, as indicated by the last digit of their masses in the subscript bracket (81) of the y-axis label, and where the asterisks indicate that all the radioactive isotopes in each of the different zones of the six sets considered, color coded as indicated in the legend box. The small dots represent each local slope at a given mass coordinate, and the large circles represent three different averages: weighted over the total mass included in each mass layer (filled circles), weighted over both the total mass and the total amount of Ni (in mass fraction) in each mass layer (empty circles), and as the previous but only including layers with Ni amounts varying within the 20th and the 80th percentile of the Ni distribution within the considered zone (i.e., with a statistical z-score lower than 1.25 (empty striped circles)).

Table 2
Main Methods and Features of the Six Sets of CCSN Models Available in the Current SIMPLE Toolkit (See Text for Details)

Set	La22	LC18	Pi16	Ra02	Ri18	Si18
			Progenitor Models			
Solar distribution[a]	GN93/L03	A09	GN93/L03	AG89	GN93/L03	L03
Evolution code	Kepler	FRANEC	GENEC	Kepler	MESA	Kepler
Nucleosynthesis code	MPPNP	FRANEC[b]	MPPNP	Kepler[b]	MPPNP	Kepler[b]
Nuclear species	5000+	300+	5000+	2200+	5000+	2200+
			Supernova Models			
Explosion engine	ν driven	Kinetic bomb	Sedov blast wave	Piston	Sedov blast wave	Piston
Mass cut	Hydro based	^{56}Ni = 0.07 $M_\odot$ with MF[c]	Fryer+12	E_{exp}=1.2 foe (for 15 $M_\odot$) ^{56}Ni = 0.1 $M_\odot$ (for 20, 25 $M_\odot$)	Fryer+12	E_{exp}=1.2 foe
Remnant mass[d] ($M_\odot$)	1.74, 2.27, 1.83	1.67, 1.66, 1.96	1.63, 2.81, 5.77	1.68, 1.55, 2.04	1.61, 2.74, 5.72	1.54, 1.58, 2.10
Nucleosynthesis code	TPPNP	FRANEC[b]	MPPNP	Kepler[b]	MPPNP	Kepler[b]
Time after explosion (s)	<200	25,000	<200	25,000	<200	25,000

Notes. As in the SIMPLE code, the labels stand for La22 = T. V. Lawson et al. (2022), LC18 = M. Limongi & A. Chieffi (2018), Pi16 = M. Pignatari et al. (2016b), Ra02 = T. Rauscher et al. (2002), Ri18 = C. Ritter et al. (2018b), Si18 = A. Sieverding et al. (2018). The sets are listed here in alphabetical order, but in the text they are in chronological order. The time after explosion is the time at which the abundances are given in the tables read by SIMPLE.

[a] Where GN93/L03 = N. Grevesse & A. Noels (1993) with the isotopic distribution of K. Lodders (2003), A09 = M. Asplund et al. (2009), AG89 = E. Anders & N. Grevesse (1989). All metallicities Z = 0.02, except for LC18, which uses Z = 0.01345.

[b] The nucleosynthesis is calculated together with the structure, either simultaneously with a fixed network (FRANEC) or after each time step with an adaptive network (Kepler).

[c] Mixing and fallback method; see the text for details.

[d] For the 15, 20, and 25 $M_\odot$ models, respectively.

The abundances are provided soon after the explosion, the exact time depending on the set: in the LC18, Ra02, and Si18 sets, the time is set to 25,000s (~7 hr), while in the other models, it is set as the time when the peak temperature decreases below approximately 1.5 GK, after which there is no more nucleosynthesis. Also note that these times are very short, and much shorter than the timescale of dust formation, probably of the order of years (E. S. Brooker et al. 2022). As mentioned above, care is therefore needed when deciding which radioactive abundances to add to the stable isotopes for each different element.

3.1. The Ra02 Set

The Ra02 set was extracted from T. Rauscher et al. (2002), where we selected the models corresponding to the publication, i.e., those labeled as S15, S20, and S25 in the publication and s15a28c, s20a28n, and s25a28d in the online database[26] (noting that the files from the first table, called expl_comp, are required for the self-consistent treatment of the radioactive decay between the code and the files). The stellar progenitors were calculated with the Kepler code (T. A. Weaver et al. 1978), adopting an initial metallicity of $Z = 0.02$ (E. Anders & N. Grevesse 1989). The explosion was simulated by the piston-driven mechanism, where a piston is placed outside the iron core, and its trajectory is calibrated by requiring a fixed kinetic energy in the ejecta measured at infinity. In the 15 $M_\odot$ model, this energy is 1.2 foe (1 foe $= 10^{51}$ erg), which corresponds to that estimated for SN 1987A. In the 20 and 25 $M_\odot$ models, instead the energy is fixed to 2.2 and 1.7 foe, respectively, to produce 0.1 $M_\odot$ of ^{56}Ni. The remnant mass (i.e., below the so-called "mass cut") for each model is determined by the solution of the piston model. The nucleosynthesis is calculated during the evolution at the end of each time step, with a large adaptive network including up to 2200 nuclear species. Note that the 20 $M_\odot$ model of this set experiences a C–O shell merger (C. Ritter et al. 2018a; L. Roberti et al. 2023, 2025) shortly before the explosion, which affects its structure and nucleosynthesis.

3.2. The Pi16 Set

The Pi16 set includes the models published in M. Pignatari et al. (2016a) and computed using the GENEC code (P. Eggenberger et al. 2008), up to the end of central Si burning. The initial metallicity is $Z = 0.02$ (N. Grevesse & A. Noels 1993), with the isotopic distribution given by K. Lodders (2003). The explosion was simulated using a semianalytical approach, with the mass-cut prescription from C. L. Fryer et al. (2012) and the L. I. Sedov (1946) blast wave (SBW) solution for the determination of the peak velocity of the shock. The initial shock velocity for each model is 2×10^9 cm s^{-1}. The maximum velocity of the shock front is capped at 5×10^9 cm s^{-1} to mimic deceleration due to viscous forces. The adiabatic cooling of the shocked material is simulated using a variant of the adiabatic exponential decay (W. A. Fowler & F. Hoyle 1964; F. Hoyle et al. 1964). The nucleosynthesis during both the evolution and the explosion is calculated by postprocessing the previously computed stellar structure using the Multi-zone Post-Processing Network—Parallel code (MPPNP; M. Pignatari & F. Herwig 2012, from the NuGrid collaboration[27]) using a dynamical network that includes more than 5000 nuclear species and more than 70,000 reactions. Note that the 25 $M_\odot$ model of this set has a rather poor resolution in mass in the O/C layer (see Section 4 for the definition), and care is needed when considering this model.

3.3. The Si18 Set

The Si18 set from A. Sieverding et al. (2018) is based on stellar models calculated using the Kepler code like the Ra02 set. The explosion is simulated by the piston-driven mechanism, imposing 1.2 foe of kinetic energy in the ejecta measured at infinity in all the three models. The nucleosynthesis is calculated as in Ra02. At variance with all the other sets, the Si18 models also include a number of updated ν-induced reactions. Since the ν-induced nucleosynthesis depends on the neutrino energy, A. Sieverding et al. (2018) presented a parametric study of the explosive yields, exploring several neutrino energies. The models included in our database are those with the highest neutrino energy, the same used in J. den Hartogh et al. (2022) and L. Roberti et al. (2023).

3.4. The Ri18 Set

The Ri18 set includes the models published in C. Ritter et al. (2018b), for which the progenitors were computed using the publicly available MESA code (e.g., B. Paxton et al. 2011). As in Pi16, the initial metallicity is $Z = 0.02$ (N. Grevesse & A. Noels 1993), with the isotopic distribution given by K. Lodders (2003). The explosions are performed as in Pi16, with the same semianalytical approach and using the same initial shock velocity of 2×10^9 cm s^{-1}. The nucleosynthesis during both the evolution and the explosion was calculated by postprocessing using the MPPNP code. Note that, like the 20 $M_\odot$ model of Ra02, the 15 $M_\odot$ model of this set experiences a C–O shell merger shortly before the explosion. The signatures of these events will be described in Section 4.

3.5. The LC18 Set

The LC18 set includes the recommended (R) models from M. Limongi & A. Chieffi (2018), calculated with the Frascati Raphson Newton Evolutionary Code (FRANEC). The initial metallicity is $Z = 0.01345$ (M. Asplund et al. 2009). While the full database[28] also includes rotating models with an initial rotational velocity of 150 and 300 km s^{-1}, here we selected only the nonrotating models. The explosion is simulated as a kinetic bomb, i.e., by injecting a certain amount of kinetic energy into the Fe core and then following the propagation of the generated shock by solving the hydrodynamic equations. While the choice of the injected energy is made to obtain the complete ejection of all the stellar layers above the Fe core, these models are also set to experience a so-called mixing and fallback (MF; H. Umeda & K. Nomoto 2002). The inner border of the mixed region is chosen by imposing that Ni/Fe $= 1.6$ (Ni/Fe)$_\odot$ and the outer border by imposing an ^{16}O mass fraction below 0.1, i.e., the mixed region cannot extend beyond the base of the oxygen shell. The amount of fallback material is then determined by requiring an ejection of 0.07 $M_\odot$ of ^{56}Ni. The nucleosynthesis is calculated during the evolution, and the isotopic composition is fully coupled to the solution of the physics and mixing equations. The nuclear network includes 335 nuclear species and more than 3000 nuclear reactions, both for the progenitor evolution and the explosion. The isotopes included a range from H to ^{209}Bi. Up to ^{98}Mo, all the possible weak and strong reactions connecting the various nuclear species are included. Above ^{98}Mo, only the neutron-capture nucleosynthesis is considered, i.e., only (n,γ) reactions and β^- decays, and only the stable and unstable isotopes around the magic numbers of neutrons $N = 82$ and $N = 126$ are explicitly included, while all the other intermediate isotopes are assumed to be at local equilibrium.

[26] https://2sn.org/nucleosynthesis/
[27] www.nugridstars.org
[28] Online Repository for the Franec Evolutionary Output (ORFEO): https://orfeo.oa-roma.inaf.it.

3.6. The La22 Set

The La22 set includes models published in S. W. Jones et al. (2019c), S. Andrews et al. (2020), and T. V. Lawson et al. (2022), which were computed using a more recent version of the Kepler code (A. Heger & S. E. Woosley 2010) compared to the progenitor models of the Ra02 and Si18 sets. Like in Pi16 and Ri18, $Z = 0.02$ (N. Grevesse & A. Noels 1993), and the isotopic distribution is from K. Lodders (2003). The explosions are modeled using a 1D hydrodynamic code that simulates the effects of the 3D convection-enhanced supernova engine of C. L. Fryer et al. (2018), exploring various explosion parameters such as power, duration, and the extent of the energy injection region within the stellar progenitors. The complete dataset includes over 60 combinations of these parameters, while the models currently included in the SIMPLE toolkit are the same as those used by J. den Hartogh et al. (2022) and L. Roberti et al. (2023). These correspond, for each initial mass, to the models with the explosion energy closest to the value of 1.2 foe used by Si18. Like for Pi16 and Ri18, the progenitor nucleosynthesis was calculated by postprocessing using the MPPNP code. The explosive nucleosynthesis was instead calculated using a different postprocessing code, the Tracer particle Post-Processing Network—Parallel code (TPPNP; S. W. Jones et al. 2019c), with the same nuclear network used for MPPNP.

4. Nickel as a Case Study

In this section, we show how to use SIMPLE to data-mine stellar models and compare the models' predictions with meteoritic data. We focus on the production of the Ni isotopes in the 20 $M_\odot$ models. Analogous figures for the 15 and 25 $M_\odot$ models are also available on Zenodo, doi:10.5281/zenodo.16743238, together with the Jupyter notebooks and the support files needed to generate them using the SIMPLE package. Here, we use the approach common in the literature of comparing CCSN models generated from stellar progenitors of the same initial mass (e.g., J. den Hartogh et al. 2022); however, we highlight that the CO core mass at the end of central He burning, which depends on the evolution of the star up to that stage, is a more reliable predictor of subsequent evolution and nucleosynthesis than the initial total stellar mass (e.g., S. E. Woosley & T. A. Weaver 1995; F.-K. Thielemann et al. 1996; A. Chieffi et al. 1998; M. Limongi & A. Chieffi 2018). For example, a 20 $M_\odot$ model in a given set could have a similar CO core mass as a 17 $M_\odot$ model in another set, making its behavior more comparable to the latter than to a 20 $M_\odot$ model from the same set. Using the CO core mass as a reference would therefore help to mitigate some of the discrepancies observed here between different models. To achieve a more consistent comparison, finer grids of stellar models should be developed in future studies.

Figure 2 shows the Ni abundance profiles for the six 20 $M_\odot$ models, and Figure 3 shows the corresponding slope of $\varepsilon^{64}\mathrm{Ni}_{(81)}$ versus $\varepsilon^{62}\mathrm{Ni}_{(81)}$ internally normalized to $^{58}\mathrm{Ni}/^{61}\mathrm{Ni}$ (see Equations (1)–(4)). In these figures, the ejecta are divided into different zones, each of which is labeled according to the classification by B. S. Meyer et al. (1995) based on the most abundant nuclear-burning products present in each zone. For example, the zone labeled as "Si" is where explosive O burning occurred, and Si is the most abundant element, while the zone labeled as "He/C" is where He burning partially occurred during the progenitor evolution, and He and C are the most abundant elements.

4.1. Description of the Stellar Structure

The width and location of the different zones defined above depend on multiple parameters, including the shell-burning processes during the presupernova evolution, the parameterization of the explosion, and the determination of the boundary between the ejecta and the remnant mass. The explosion primarily affects the definition and the width of Ni, Si, and O/Si zones and the location of the inner boundary of the O/Ne zone, while the outer boundary of the O/Ne zone, as well as the O/C, He/C, He/N, and H zones, are solely determined by the presupernova evolution. The inner boundary of the O/C zone defines the size of the CO core, which slightly changes after He burning, but still serves as a reliable indicator of the characteristics of the star (e.g., W. D. Arnett & F. K. Thielemann 1985). In our dataset, the inner border of the O/C zone varies in the range ~3.4−4.5 $M_\odot$, resulting in a variation of about 1 $M_\odot$ among different models. Differences in presupernova evolution are also evident in the outer regions of the O/Ne zone. This region contains the ashes of the convective carbon shell, and variations in stellar evolution result in different chemical compositions, which can ultimately influence the slope plotted in Figure 3 within this zone. While variations in the Ni isotopes are relatively small, the impact may be more significant for other elements. Another important difference is that the Ra02 model undergoes a C–O shell merger during presupernova evolution. This event leads to the removal of the O/Ne zone, as the merging of the carbon-burning shell with the oxygen-burning shell enhances the Si produced by the oxygen burning. As a result, this model exhibits only a large O/Si zone. Among the remaining models, this peculiar occurrence is observed only in the 15 $M_\odot$ model in the Ri18 set.

The different methods used to simulate the supernova explosion impact both the boundaries of the ejecta, as variations in fallback prescriptions and mass-cut choices significantly influence the final remnant mass, while the explosion prescription can influence the upper boundary of the ejecta. For the 20 $M_\odot$ models, the remnant mass varies between 1.55 and 2.81 $M_\odot$. In the most extreme case, all the zones below the O/Ne are locked within the remnant.

Some special events in the progenitor models might change the abundance profiles, and also for the most abundant species, defying the standard zone classification used here following B. S. Meyer et al. (1995). For instance, the Pi16 15 $M_\odot$ model developed a so-called C/Si zone in between the O/C zone and the He/C zone (see also M. Pignatari et al. 2013). In several models calculated from the Pi16 25 $M_\odot$ model (not included in the SIMPLE current set), an O-rich O/nova zone develops close to the bottom of the He/C zone (M. Pignatari et al. 2015, 2018). We do not account for special cases in the current SIMPLE ejecta structure visualization package, and this will need to be updated to capture exotic zones produced by the simulations, especially as more models will be included in the future. New nucleosynthesis components identified in CCSN ejecta may indeed prove crucial for understanding the isotopic heritage of the solar system. Although still highly uncertain, CCSN-derived presolar grains could account for up to 30% of the presolar stardust that contributed to the protosolar nebula (P. Hoppe et al. 2022). Among these, a nonnegligible fraction

appears best explained by exotic models rather than by more standard CCSN yield sets. Hints of these puzzling compositions may also be reflected in CAIs (e.g., K. Larsen et al. 2020).

4.2. Description of the Ni Composition

The Ni stable isotopes show a rich and diverse nucleosynthesis both in hydrostatic and CCSN conditions, resulting in a large range of variations in their abundances in the final ejecta. Explosive Si burning efficiently produces ^{58}Ni, ^{61}Ni, and ^{62}Ni; explosive O burning mostly makes ^{58}Ni; and the combination of the *slow* neutron-capture (*s*) process during the progenitor evolution with the explosive neutron bursts in the convective C and He shells produces ^{60}Ni, ^{61}Ni, ^{62}Ni, and ^{64}Ni (e.g., S. E. Woosley et al. 2002; M. Pignatari et al. 2016a). To ensure the physical significance of the slopes plotted in Figure 3, it is useful to use Figure 2 to verify for each region of the ejecta that the abundance of one or more isotopes is not depleted by orders of magnitude, or even approaching zero, relative to their corresponding initial, i.e., surface, abundances. In this case, while it would still be possible to calculate a slope, there would be no material to carry its signal. While this consideration is not particularly relevant for Ni, which is generally abundantly produced in CCSNe, it must be carefully taken into account when examining elements with isotopes more scarcely produced, such as those heavier than Fe.

Figures 2 and 3 were generated by adding the abundances of all the radioactive isotopes listed in Table 1 to the stable Ni isotopes. While most of these isotopes decay in a less than a day, the decay chain ^{60}Fe(β^-)^{60}Co(β^-)^{60}Ni has much longer half-lives (5.27 yr for ^{60}Co, and 2.62 million years for ^{60}Fe). Therefore, these isotopes may not contribute to the abundance of ^{60}Ni, depending on the dust formation time and the chemical behavior of these elements in different dust. For practical purposes, this is not relevant to the slopes shown in Figure 3 because ^{60}Ni is not included in the calculation of the ε values considered there. In general, isotopes such as ^{60}Ni with a potentially high radiogenic component require extra care when determining the origin of their variability to avoid confusion between the radiogenic and nucleosynthetic isotope variations. Here, we use this prominent example simply to illustrate how the evaluation of the impact of radioactive decay can be easily performed using the SIMPLE code by producing plots such as Figure 1, which shows which fraction of the abundance of ^{60}Ni is due to the decay of its radioactive parents, especially ^{60}Fe, and in which region of the ejecta.

The different explosion methods impact the Ni distribution differently in each of the zones defined above. The Ni-rich zone is the most internal zone of the ejecta, which contains material processed at very high temperatures ($\geqslant$5 GK); it is where the matter evolves at the nuclear statistical equilibrium (NSE). The different approaches used in the different codes to simulate this high temperature regime lead to a large difference in the Ni isotope distribution and in the slope. Conversely, all the models ejecting a Si zone have similar abundances of Ni isotopes (and therefore similar slopes), with a larger production of the neutron deficient nuclei ^{58}Ni and ^{60}Ni relative to the more neutron-rich isotopes, due to the high efficiency of photodisintegration in this zone. The Ni outcomes of the O/Si zone depend on whether the star experienced a C–O shell merger and whether the explosion efficiently activated the ^{22}Ne(α,n)^{25}Mg reaction, triggering an explosive neutron burst. As already mentioned, the C–O shell merger alters the external part of the O/Si zone, while the neutron burst enhances the production of ^{64}Ni relative to ^{61}Ni. In models where the neutron burst does not occur, these two nickel isotopes are coproduced in similar proportions. From the O/Ne zone, there is no signature of explosive nucleosynthesis, except in those models where the shock wave is able to be efficiently revived due to the density drop at the O/C zone interface. In these cases, some explosive He burning can occur, together with the explosive neutron burst. The models without explosive He burning instead have only slight traces of the hydrostatic *slow* neutron-capture process in the O/C and He/C zones.

A summary of the slopes from all the model sets for 20 $M_\odot$ is shown in Figure 4, organized by zone, including both the local slopes at each ejected mass coordinate and three different weighted averaged values. Single mass coordinates within the same zone can produce extremely variable results including outliers, some of which are located outside the figure boundary. The plotted averages are more representative of the Ni isotopic production in each zone. The figure shows the different signatures discussed above: neutron-capture processes in the He/C region, the broad production signatures in the O/C and O/Ne zones, and variations in the O/Si zone to several nucleosynthesis components present in these parts of the ejecta, from charged particle reactions in explosive Ne burning and partial O burning (e.g., A. Chieffi et al. 1998) to neutron captures during explosive C burning (M. Pignatari et al. 2016a) and the γ-process (e.g., L. Roberti et al. 2023, 2024). The He/N and the Si zones show the smallest variations in the slope among all the different models.

In the He/N zone, this is due to the fact that the temperatures are not high enough to efficiently affect the Ni isotopes. Here, the plotted results are driven by marginal production or destruction of some of the Ni isotopes. The small dispersion of the data at some ejected mass coordinates of the 15 and 20 $M_\odot$ models is a good diagnostic of some active nucleosynthesis. However, it is unlikely that any realistic dilution factor would allow such small signatures to be preserved. It is also possible that the small anomaly seen in this region is driven by numerical errors introduced in the stellar calculations, where rounding numbers for the initial abundances and/or internal condition for mass conservation may generate small departures from the reference solar abundances. In general, we conclude that slopes obtained in the He/N zone should be considered with caution, except for a few light elements like CNO, which are affected by nucleosynthesis in this region. In the Si zone, instead, the Ni isotopes are strongly affected. Therefore, the fact that all the models able to eject a Si zone, independently from the progenitor mass and stellar set, provide us with a slope of $\sim$3 is a robust result. As described above and noted by R. C. J. Steele et al. (2012) and D. L. Cook et al. (2021), this result depends on the fact that, in this region, ^{58}Ni is the strongly favored isotope, which inevitably results in a slope of $\sim$3, when internally normalized and calculated relative to the solar abundances. Therefore, we also conclude that, when considering CCSNe as a source of the Ni anomaly, while the significant variability could provide a slope compatible with the observations in most of the ejecta, the most likely scenario is that they originated from an ejected Si zone.

5. Summary, Discussion, Conclusions, and Future Work

We have presented the new Python tool SIMPLE, which comprises both software and a large collection of input data, as needed to compare stellar abundances in the ejecta of Fe-CCSNe to meteoritic data. We provide input data from 18 models of solar metallicity, three different initial masses (15, 20, and 25 $M_{\odot}$), and six different sets (published in 2002, 2016, 2018, and 2022) to be able to reach more robust results than ever before. The code handles radioactive decay by allowing the addition of the full abundances of unstable nuclei to their stable daughter nuclei. A more accurate implementation of the radioactive exponential law following a time evolution after the explosion will be implemented in the future. The code also allows calculation from stellar predictions of the correlation between isotopic ratios of different elements, with some basic implementation on the possible choice of the chemical fraction between two elements. While this was not the focus of our current presentation, we note that, with minimal modification, the code can also be used for other applications, for instance, to calculate integrated abundance yields and/or to plot quantities useful for the comparison to stardust grains, from isotopic ratios to per mil variations relative to solar (δ-values, e.g., J. den Hartogh et al. 2022).

As an illustrative case of the capabilities of SIMPLE, we have used the isotopes of Ni. We have described in detail the similarities and the peculiarities of the different models to provide a guideline for future studies on other elements. We confirm previous results (R. C. J. Steele et al. 2012; D. L. Cook et al. 2021; T. Hopp et al. 2022) based on four models, only that the observed Ni variations in bulk meteorites can be robustly matched by material produced in the Si zone of CCSN ejecta.

SIMPLE can be easily extended to incorporate stellar abundance predictions from more models. Specifically for CCSNe, the current grid could be extended to results based on 3D prescriptions (e.g., A. Sieverding et al. 2023), to more masses, for a more consistent comparison using the CO core rather than the initial mass (as discussed at the start of Section 4), as well as more explosion parameters, for example, by adding the other >60 models published in the La22 set. In general, it is debated which initial masses explode as CCSNe (e.g., M. Ugliano et al. 2012; T. Ertl et al. 2016; T. Sukhbold et al. 2016; L. Boccioli & L. Roberti 2024), and while lower masses are more common, higher masses eject more mass; therefore, it will be useful to also extend the range of masses of the input models. Other sources to consider may be novae (e.g., P. A. Denissenkov et al. 2014) and other types of supernovae, such as thermonuclear supernovae (e.g., J. D. Keegans et al. 2023) and ECSNe (S. Jones et al. 2019b), as well as the nucleosynthetic outcomes of specific explosion-related processes, such as neutrino winds, and for the stellar wind of massive stars (e.g., S. Jones et al. 2016; M. Pignatari et al. 2016a; C. Ritter et al. 2018b; H. E. Brinkman et al. 2021). Predictions from intermediate- and low-mass stars in the AGB phase (e.g., U. Battino et al. 2016; A. I. Karakas & M. Lugaro 2016; M. Pignatari et al. 2016a) could also be added as input to the code.

Finally, to obtain a broader view of the compositions achievable in CCSNe, mixing of different mass layers (both adjacent and not) is another feature that will be useful to implement in the code, similarly to what has been done recently to study supernova light curves (C. L. Fryer et al. 2023; A. E. Niblett et al. 2025). We aim for the SIMPLE code to represent a collaborative tool, welcome collaboration on its development, and plan to pursue its dissemination.

Acknowledgments

The authors thank the anonymous reviewer for the comments. This work was supported by the European Union's Horizon 2020 research and innovation program (ChETEC-INFRA—Project no. 101008324), the Lendület Program LP2023-10 of the Hungarian Academy of Sciences, the Hungarian NKFIH via K-project 138031 and NKKP Advanced grant 153697, and the IReNA network by NSF AccelNet (grant No. OISE-1927130). G.G.B. thanks the support provided by the undergraduate research assistant program of Konkoly Observatory. M.L. was also supported by the NKFIH excellence grant TKP2021-NKTA-64. M.P. thanks the support from the ERC Synergy Grant Programme (Geoastronomy, grant agreement number 101166936, Germany). Work by A.S. was performed under the auspices of the U.S. Department of Energy by Lawrence Livermore National Laboratory under contract DE-AC52-07NA27344. Lawrence Livermore National Security, LLC. This research was supported by NuGrid (https://nugrid.github.io/), and it used the Astrohub online virtual research environment (https://astrohub.uvic.ca), developed and operated by the Computational Stellar Astrophysics group (http://web.uvic.ca/~fherwig) at the University of Victoria and hosted on the Computed Canada Arbutus Cloud at the University of Victoria. L.R. acknowledges the support from the PRIN URKA grant No. `prin_2022rjlwhn` and from the INAF grant GO-GTO2024 "Pre-supernova outbursts in Galactic RSGs".

ORCID iDs

Marco Pignatari https://orcid.org/0000-0002-9048-6010
Mattias Ek https://orcid.org/0000-0002-2327-7286
Georgy V. Makhatadze https://orcid.org/0000-0002-9182-3015
Gábor G. Balázs https://orcid.org/0009-0003-0702-8129
Lorenzo Roberti https://orcid.org/0000-0003-0390-8770
James M. Ball https://orcid.org/0009-0009-1442-2005
Borbála Cseh https://orcid.org/0000-0002-6497-8863
Alessandro Chieffi https://orcid.org/0000-0002-3589-3203
Chris Fryer https://orcid.org/0000-0003-2624-0056
Falk Herwig https://orcid.org/0000-0001-8087-9278
Marco Limongi https://orcid.org/0000-0003-0636-7834
Thomas Rauscher https://orcid.org/0000-0002-1266-0642
Maria Schönbächler https://orcid.org/0000-0003-4304-214X
Reto Trappitsch https://orcid.org/0000-0002-0924-236X
Maria Lugaro https://orcid.org/0000-0002-6972-3958

References

Akram, W., & Schönbächler, M. 2016, E&PSL, 449, 302
Anders, E., & Grevesse, N. 1989, GeCoA, 53, 197
Andrews, S., Fryer, C., Even, W., Jones, S., & Pignatari, M. 2020, ApJ, 890, 35
Arnett, W. D., & Thielemann, F. K. 1985, ApJ, 295, 589
Asplund, M., Grevesse, N., Sauval, A. J., & Scott, P. 2009, ARA&A, 47, 481
Battino, U., Pignatari, M., Ritter, C., et al. 2016, ApJ, 827, 30
Bermingham, K., & Meyer, B. 2024, Oeps Book (Oxford Univ. Press)
Bermingham, K. R., Füri, E., Lodders, K., & Marty, B. 2020, SSRv, 216, 133
Bizzarro, M., Johansen, A., & Dorn, C. 2025, NRvCh, 9, 711
Boccioli, L., & Roberti, L. 2024, Univ, 10, 148

Brennecka, G. A., Borg, L. E., & Wadhwa, M. 2013, PNAS, 110, 17241
Brinkman, H. E., den Hartogh, J. W., Doherty, C. L., Pignatari, M., & Lugaro, M. 2021, ApJ, 923, 47
Brooker, E. S., Stangl, S. M., Mauney, C. M., & Fryer, C. L. 2022, ApJ, 931, 85
Burkhardt, C., Spitzer, F., Morbidelli, A., et al. 2021, SciA, 7, eabj7601
Burrows, A., & Vartanyan, D. 2021, Natur, 589, 29
Chieffi, A., Limongi, M., & Straniero, O. 1998, ApJ, 502, 737
Cook, D. L., Meyer, B. S., & Schönbächler, M. 2021, ApJ, 917, 59
Dauphas, N., Chen, J. H., Zhang, J., et al. 2014, E&PSL, 407, 96
Dauphas, N., Davis, A. M., Marty, B., & Reisberg, L. 2004, E&PSL, 226, 465
Dauphas, N., Marty, B., & Reisberg, L. 2002, ApJ, 565, 640
Dauphas, N., & Schauble, E. A. 2016, AREPS, 44, 709
den Hartogh, J., Petö, M. K., Lawson, T., et al. 2022, ApJ, 927, 220
Denissenkov, P. A., Truran, J. W., Pignatari, M., et al. 2014, MNRAS, 442, 2058
Eggenberger, P., Meynet, G., Maeder, A., et al. 2008, Ap&SS, 316, 43
Ek, M., Hunt, A. C., Lugaro, M., & Schönbächler, M. 2020, NatAs, 4, 273
Ertl, T., Janka, H. T., Woosley, S. E., Sukhbold, T., & Ugliano, M. 2016, ApJ, 818, 124
Fowler, W. A., & Hoyle, F. 1964, ApJS, 9, 201
Fryer, C. L., Andrews, S., Even, W., Heger, A., & Safi-Harb, S. 2018, ApJ, 856, 63
Fryer, C. L., Belczynski, K., Wiktorowicz, G., et al. 2012, ApJ, 749, 91
Fryer, C. L., Burns, E., Hungerford, A., et al. 2023, ApJ, 956, 19
Fryer, C. L., Schatz, H., Jones, S., et al. 2026, arXiv:2601.04464
Grevesse, N., & Noels, A. 1993, in Origin and Evolution of the Elements, ed. N. Prantzos, E. Vangioni-Flam, & M. Casse (Cambridge Univ. Press), 15
Heger, A., & Woosley, S. E. 2010, ApJ, 724, 341
Hopp, T., Dauphas, N., Spitzer, F., Burkhardt, C., & Kleine, T. 2022, E&PSL, 577, 117245
Hoppe, P., Leitner, J., Kodolányi, J., Borrmann, S., & Jones, A. P. 2022, NatAs, 6, 1027
Hoyle, F., Fowler, W. A., Burbidge, G. R., & Burbidge, E. M. 1964, ApJ, 139, 909
Hutchison, M. A., Bodénan, J.-D., Mayer, L., & Schönbächler, M. 2022, MNRAS, 512, 5874
Iizuka, T., Hibiya, Y., Yoshihara, S., & Hayakawa, T. 2025, ApJL, 979, L29
Jones, S., Côté, B., Röpke, F. K., & Wanajo, S. 2019a, ApJ, 882, 170
Jones, S., Ritter, C., Herwig, F., et al. 2016, MNRAS, 455, 3848
Jones, S., Röpke, F. K., Fryer, C., et al. 2019b, A&A, 622, A74
Jones, S. W., Möller, H., Fryer, C. L., et al. 2019c, MNRAS, 485, 4287
Karakas, A. I., & Lugaro, M. 2016, ApJ, 825, 26
Keegans, J. D., Pignatari, M., Stancliffe, R. J., et al. 2023, ApJS, 268, 8
Kleine, T., Budde, G., Burkhardt, C., et al. 2020, SSRv, 216, 55
Kruijer, T. S., Burkhardt, C., Budde, G., & Kleine, T. 2017, PNAS, 114, 6712
Kruijer, T. S., Kleine, T., & Borg, L. E. 2020, NatAs, 4, 32
Larsen, K., Wielandt, D., Schiller, M., Krot, A., & Bizzarro, M. 2020, E&PSL, 535, 116088
Lawson, T. V., Pignatari, M., Stancliffe, R. J., et al. 2022, MNRAS, 511, 886
Lichtenberg, T., Drazkowska, J., Schönbächler, M., Golabek, G. J., & Hands, T. O. 2021, Sci, 371, 365
Limongi, M., & Chieffi, A. 2018, ApJS, 237, 13
Limongi, M., Roberti, L., Chieffi, A., & Nomoto, K. 2024, ApJS, 270, 29
Liu, N., Lugaro, M., Leitner, J., Meyer, B. S., & Schönbächler, M. 2024, SSRv, 220, 88
Lodders, K. 2003, ApJ, 591, 1220
Lugaro, M., Karakas, A. I., & Flavia, D. 2023, in Chemical Element and Dust Production in AGB Stars, ed. S. Amari (Elsevier)
Meyer, B. S., Weaver, T. A., & Woosley, S. E. 1995, Metic, 30, 325
Mezger, K., Schönbächler, M., & Bouvier, A. 2020, SSRv, 216, 1
Nanne, J. A. M., Nimmo, F., Cuzzi, J. N., & Kleine, T. 2019, E&PSL, 511, 44
Niblett, A. E., Fryer, D. A., & Fryer, C. L. 2025, ApJ, 994, 259
Niemeyer, S., & Lugmair, G. W. 1981, E&PSL, 53, 211
Nittler, L. R., O'D. Alexander, C. M., Liu, N., & Wang, J. 2018, ApJL, 856, L24
Paxton, B., Bildsten, L., Dotter, A., et al. 2011, ApJS, 192, 3
Pignatari, M., Göbel, K., Reifarth, R., & Travaglio, C. 2016a, IJMPE, 25, 1630003
Pignatari, M., & Herwig, F. 2012, NPNew, 22, 18
Pignatari, M., Herwig, F., Hirschi, R., et al. 2016b, ApJS, 225, 24
Pignatari, M., Hoppe, P., Trappitsch, R., et al. 2018, GeCoA, 221, 37
Pignatari, M., Wiescher, M., Timmes, F. X., et al. 2013, ApJ, 767, L22
Pignatari, M., Zinner, E., Hoppe, P., et al. 2015, ApJL, 808, L43
Qin, L., & Carlson, R. W. 2016, GeocJ, 50, 43
Qin, L., Nittler, L. R., Alexander, C. M. O. D., et al. 2011, GeCoA, 75, 629
Rauscher, T., Heger, A., Hoffman, R. D., & Woosley, S. E. 2002, ApJ, 576, 323
Ritter, C., Andrassy, R., Côté, B., et al. 2018a, MNRAS, 474, L1
Ritter, C., Herwig, F., Jones, S., et al. 2018b, MNRAS, 480, 538
Roberti, L., Pignatari, M., Brinkman, H. E., et al. 2025, A&A, 698, A216
Roberti, L., Pignatari, M., Fryer, C., & Lugaro, M. 2024, A&A, 686, L8
Roberti, L., Pignatari, M., Psaltis, A., et al. 2023, A&A, 677, A22
Rotaru, M., Birck, J. L., & Allegre, C. J. 1992, Natur, 358, 465
Russell, W. A., Papanastassiou, D. A., & Tombrello, T. A. 1978, GeCoA, 42, 1075
Schiller, M., Bizzarro, M., & Fernandes, V. A. 2018, Natur, 555, 507
Schönbächler, M., Bouvier, A., Kita, N. T., & Kruijer, T. S. 2025, SSRv, 221, 97
Sedov, L. I. 1946, ApMM, 10, 241
Sieverding, A., Kresse, D., & Janka, H.-T. 2023, ApJL, 957, L25
Sieverding, A., Martínez-Pinedo, G., Huther, L., Langanke, K., & Heger, A. 2018, ApJ, 865, 143
Simon, J. I., DePaolo, D. J., & Moynier, F. 2009, ApJ, 702, 707
Steele, R. C. J., Coath, C. D., Regelous, M., Russell, S., & Elliott, T. 2012, ApJ, 758, 59
Sukhbold, T., Ertl, T., Woosley, S. E., Brown, J. M., & Janka, H. T. 2016, ApJ, 821, 38
Thielemann, F.-K., Nomoto, K., & Hashimoto, M.-A. 1996, ApJ, 460, 408
Tissot, F. L. H., Burkhardt, C., Kuznetsova, A., et al. 2025, SSRv, 221, 85
Trinquier, A., Elliott, T., Ulfbeck, D., et al. 2009, Sci, 324, 374
Ugliano, M., Janka, H.-T., Marek, A., & Arcones, A. 2012, ApJ, 757, 69
Umeda, H., & Nomoto, K. 2002, ApJ, 565, 385
van Kooten, E., Schiller, M., Moynier, F., et al. 2021, ApJ, 910, 70
Van Kooten, E. M. M. E., Wielandt, D., Schiller, M., et al. 2016, PNAS, 113, 2011
Weaver, T. A., Zimmerman, G. B., & Woosley, S. E. 1978, ApJ, 225, 1021
Woosley, S. E., & Heger, A. 2007, PhR, 442, 269
Woosley, S. E., Heger, A., & Weaver, T. A. 2002, RvMP, 74, 1015
Woosley, S. E., & Weaver, T. A. 1995, ApJS, 101, 181
Yokoyama, T., & Walker, R. J. 2016, RvMG, 81, 107
Zinner, E. 2014, in Meteorites and Cosmochemical Processes. Vol. 1 Treatise on Geochemistry, ed. A. M. Davis & H. D. Holland (2nd Ed.; Elsevier), 181